

¹ Modeling the growth of stylolites in sedimentary ² rocks.

Alexandra Rolland^{1,2}, Renaud Toussaint¹, Patrick Baud¹, Jean Schmittbuhl¹,
Nathalie Conil², Daniel Koehn³, François Renard^{4,5}, Jean-Pierre Gratier⁴

Alexandra Rolland, Institut de Physique du Globe, Université de Strasbourg, 5 rue René Descartes, 67084 cedex, Strasbourg, France (alexandra.rolland@unistra.fr)

Renaud Toussaint, Institut de Physique du Globe, Université de Strasbourg, 5 rue René Descartes, 67084 cedex, Strasbourg, France (renaud.toussaint@unistra.fr)

Patrick Baud, Institut de Physique du Globe, Université de Strasbourg, 5 rue René Descartes, 67084 cedex, Strasbourg, France (patrick.baud@unistra.fr)

Jean Schmittbuhl, Institut de Physique du Globe, Université de Strasbourg, 5 rue René Descartes, 67084 cedex, Strasbourg, France (jean.schmittbuhl@unistra.fr)

Nathalie Conil, Agence Nationale pour la gestion des Déchets Radioactifs, Centre de Meuse/Haute-Marne, Route Départementale 960, BP 9, 55290, Bure, France

Daniel Koehn, University of Glasgow, Scotland

François Renard, ISTerre, Université Joseph Fourier, Grenoble, France

Jean-Pierre Gratier, ISTerre, Université Joseph Fourier, Grenoble, France

¹Institut de Physique du Globe,

³ **Abstract.** Stylolites are ubiquitous pressure-solution seams found in sed-
⁴ imentary rocks. Their morphology is shown to follow two self-affine regimes:
⁵ analyzing the scaling properties of their height over their average direction
⁶ shows that at small scale, they are self-affine surfaces with a Hurst exponent
⁷ around 1, and at large scale, they follow another self-affine scaling with Hurst
⁸ exponent around 0.5. In the present paper we show theoretically the influ-
⁹ ence of the main principal stress and the local geometry of the stylolitic in-
¹⁰ terface on the dissolution reaction rate. We compute how it is affected by
¹¹ the deviation between the principal stress axis, and the local interface be-
¹² tween the rock and the soft material in the stylolite. The free energy enter-
¹³ ing in the dissolution reaction kinetics is expressed from the surface energy
¹⁴ term, and via integration from the stress perturbations due to these local mis-
¹⁵ alignments. The resulting model shows the interface evolution at different stress
¹⁶ conditions. In the stylolitic case, i.e. when the main principal stress is nor-

Université de Strasbourg, France

²Andra, Bure, France

³School of Geographical and Earth
Sciences, University of Glasgow, France

⁴ISTerre, University Joseph Fourier -
Grenoble I and CNRS, France

⁵PGP, University of Oslo, Norway

mal to the interface, two different stabilizing terms dominate at small and large scales which are linked respectively to the surface energy and to the elastic interactions. Integrating the presence of small scale heterogeneities related to the rock properties of the grains in the model leads to the formulation of a Langevin equation predicting the dynamic evolution of the surface. This equation leads to saturated surfaces obeying the two observed scaling laws. Analytical and numerical analysis of this surface evolution model shows that the cross-over length separating both scaling regimes depends directly on the applied far-field stress magnitude. This method gives the basis for the development of a paleostress magnitude marker. We apply the computation of this marker, i.e. the morphological analysis, on a stylolite found in the Dogger limestone layer located in the neighborhood of the Andra Underground Research Laboratory at Bure (Eastern France). The results are consistent with the two scaling regimes expected, and the practical determination of the major principal paleostress, from the estimation of a cross-over length, is illustrated on this example.

1. Introduction

Stylolites are undulated surfaces resulting from localized stress-driven dissolution of some minerals of the rock. Insoluble minerals as clay particles, oxides and organic matters are concentrated in the interface and make stylolites visible. *Bathurst* [1987] describes stylolites as serrated interfaces with an amplitude greater than the diameter of the transected grains giving them a sutured appearance. He makes a difference with dissolution seams or 'flaser' which are smooth, undulating, lacking in sutures and fitting around grains instead of cutting through them. Stylolites are most often found in carbonates [*Stockdale*, 1922, 1926, 1936, 1943; *Dunnington*, 1954; *Bushinskiy*, 1961; *Park and Schot*, 1968; *Bathurst*, 1971; *Buxton and Sibley*, 1981; *Railsback*, 1993] but also in sandstones [*Young*, 1945; *Heald*, 1955], shales [*Wright and Platt*, 1982; *Rutter*, 1983], cherts [*Bushinskiy*, 1961; *Iijima*, 1979; *Cox and Whitford-Stark*, 1987] and sometimes in coal [*Stutzer*, 1940]. Stylolites are divided in two groups according (i) to their orientation with respect to the bedding of the surrounding rock or (ii) to the orientation of their 'tooth' with respect to the mean plane of the stylolite. The first group shows two types of orientation: stylolites parallel to the bedding plane, designated as sedimentary, and formed under the lithostatic pressure and stylolites oblique or even perpendicular to the bedding, designated as tectonic, and depending on the maximum tectonic stress. The tooth orientation is in both cases an indicator of the direction of the incremental displacement which is parallel to the major principal stress in co-axial deformation. The stylolites of the second group are called 'slickolites' [*Ebner et al.*, 2010a]. They develop when there is a preferential plane for their growth (bedding or fracture). In this case, the stress is not perpendicular to the

mean plane of the stylolite [Stockdale, 1922], but the edges of the tooth are subparallel to the maximum principal stress axis. Various studies [Park and Schot, 1968; Renard et al., 1997, 2001; André, 2003; Aharonov and Katsman, 2009] suggest that many parameters play an important role in the stylolite growth such as confining pressure, deviatoric stress, fluid pressure, temperature, shape and assemblage of grains, anisotropy of minerals, rates of dissolution and presence of clay (acting potentially as catalyst for the dissolution).

Only few papers report experiments about stylolites development. Indeed, they are inherently difficult to reproduce as the kinetics of pressure-solution processes is very slow [Rutter, 1976]. Experiments were conducted either on aggregates [Cox and Paterson, 1991; Den Brok and Morel, 2001; Renard et al., 2001; Gratier et al., 2005] or with indenter techniques [Gratier and Guiguet, 1986; Gratier, 1993; Gratier et al., 2004; Dysthe et al., 2002, 2003; Karcz et al., 2008]. Dysthe et al. [2002, 2003] used an indenter technique where a sodium chloride crystal was kept in contact with a piston at given pressure and temperature for several months. A fluid at compositional equilibrium with the crystal is trapped between the sample and the indenter. The contact evolved due to pressure-solution during the indentation. A power law time dependence with an exponent value of $1/3$ as in Andrade creep law was shown to control the indentation rate. The observed microstructures in the contact seem to be different from stylolites. Karcz et al. [2008] loaded a halite cone-shaped indenter against a flat silicate surface immersed in an undersaturated brine. Using confocal microscopy techniques, they observed that the evolution of the system is dictated by an interaction between two deformation mechanisms: undercutting dissolution reducing the area of the contact and plastic flow increasing it. Recently, similar experiments were carried out with a brine at chemical equilibrium with the crystal

77 [*Laronne Ben-Itzhak*, 2011]. Emerging evolving islands and channels were observed at
78 the contact. Such islands and channels structures were previously observed at the con-
79 tacts during experiments on aggregates [*Schutjens and Spiers*, 1999; *Den Brok and Spiers*,
80 1991]. Other experiments on aggregates were performed by *Gratier et al.* [2005]. They
81 loaded layers of fine quartz sand grains. The experiments lasted several months at 350°C,
82 under 50 MPa of differential stress and in presence of an aqueous silica solution. Microsty-
83 lolites were created for the first time in the laboratory at the stressed contacts between the
84 quartz grains. An interesting observation is that the stylolites peaks are always located
85 in front of dislocation pits. Consequently, stylolites appear to be localized by the hetero-
86 geneities of the mineral. *Den Brok and Morel* [2001] loaded elastically K-alum crystals at
87 a controled temperature and in a saturated K-alum solution. A hole was drilled in the
88 middle of the crystals to provide an elastic strain gradient. They observed macroscopic
89 etch grooves on the originally smooth free surfaces of the soluble crystals which disappear
90 when removing the stress. *Koehn et al.* [2004] stressed crystals of $NaClO_3$ in a $NaClO_3$
91 solution at room temperature. Parallel dissolution grooves developed on their free surface
92 in a 1D geometry to a 2D geometry with the coarsening of the pattern. The pressure-
93 solution process slowed down or stopped progressively with the increasing concentration
94 of the solution during the experiments. *Gratier et al.* [2004] used a similar technique in
95 which a sample of Bure claystone was kept in contact with a piston, with a saturated
96 brine in the contact, at an imposed pressure and temperature for several months. No
97 evidence of localized pressure-solution (dissolution seam) was observed in this case, grain
98 to grain sliding being more efficient in presence of clay. *Renard et al.* [2001], studied
99 chemical compaction of aggregates of halite (salt) mixed with clay. They showed that

100 clay particles enhance pressure-solution. Moreover, *Renard et al.* [1997] studied the effect
101 of clay on clay-rich sandstones. They suggested that pressure-solution is enhanced by clay
102 because a thick film of water is preserved between clay particles. They also concluded
103 that the depth determines the limiting factor for the process: at great depth, the water
104 film between grains should be thinner and diffusion limits the process. Conversely, at low
105 depth water films are bigger, transport is easier and the reaction kinetics is the limiting
106 factor.

107 The clay particles effect on pressure-solution was recently simulated in numerical mod-
108 eling. *Aharonov and Katsman* [2009] used the two-dimensional Spring Network Model to
109 study the stylolites growth in a medium with a uniform clay distribution. They showed
110 that clay plays a role of enhancing pressure-solution and that stylolites propagation is
111 possible only when both pressure-solution and clay-enhanced dissolution operate together.
112 *Koehn et al.* [2007] developed a new discrete simulation technique that reproduces suc-
113 cessfully the roughening of stylolites from a preferential existing surface with no clay. This
114 model is based on molecular dynamics, with a dissolution speed depending on the local
115 free energy that includes stress dependent terms and surface energy terms. Two different
116 spatial regimes arise from this modeling: a small-scale regime where surface energy is
117 dominant with significant fluctuations of the roughness and a large-scale regime where
118 elastic energy dominates. The dependence on the cross-over scale between both regime
119 on the imposed stress has been recently investigated numerically [*Koehn*, 2012]. This
120 model shows that the growth of the stylolite tooth follows the main compressive stress
121 direction. The nature and structure of the small scale disorder for the dissolution prop-
122 erties of grains were systematically analyzed [*Ebner et al.*, 2009a]. Moreover, *Ebner et al.*

[2010b] performed detailed microstructural analysis to investigate the interplay between this disorder and the compositional nature of the grains surrounding a stylolite.

Stylolites are localised features for which deformation is purely compactant as for compaction bands [Mollema and Antonellini, 1996; Baud *et al.*, 2004; Katsman *et al.*, 2006b; Tembe *et al.*, 2008]. Stylolites and compaction bands development was modeled as anticracks or anti-mode I fracture [Fletcher and Pollard, 1981; Rispoli, 1981; Mollema and Antonellini, 1996]. Fletcher and Pollard [1981] assume that the rate of pressure-solution is only a function of the normal stress. They observed an elliptic dissolution pattern i.e. more dissolution in the central part of stylolites than at the tips. With these observations they proposed an analogy between propagation of stylolites and propagation of mode I fractures. They observed that the relative displacement between the sides of a stylolite should have the opposite sign than that of a crack, and thus termed their model an anticrack. Note however that cracks can bear zero surface traction, contrary to stylolites. This distinction between crack solutions and stylolites was introduced, and it was shown by Katsman *et al.* [2006a] that, as compaction bands, stylolites are Localized Volume Reduction zones (LVR). The shape of the displacement along stylolites, and how the stress perturbation can be determined from the concept of LVR, is discussed in details by Katsman [2010].

In LVR where the dissolution amount is constant across the surface of the LVR, as for a compaction band, the stress enhancement was shown to be that of a dislocation [Katsman *et al.*, 2006a]. In later models Katsman [2010], it was shown that if more dissolution is allowed in the center of a stylolite, another type of stress enhancement, with a dependence on the distance to the tips analogous to the one for a crack (rather than to a dislocation),

146 can be observed it is given by the Eshelby inclusion problem. Such an increase of the
147 dissolution in the center of a stylolite, where the dissolution does not stop in the already
148 dissolved zone in the middle of the stylolite, can be observed in models with a positive
149 feedback do the dissolution, as for example the one that can be modeled from a clay
150 concentration mechanism [Aharonov and Katsman, 2009].

151 In general, in stylolites, the stress concentrates at the tips and the largest stress is
152 perpendicular to the stylolites. Recent models [Koehn et al., 2007; Ebner et al., 2009b;
153 Zhou and Aydin, 2010] suggest that a higher stress concentration at the top of the tooth
154 should be responsible of localized high rates of dissolution. Benedicto and Schultz [2010]
155 investigated the topography of stylolites (along-strike trace length, maximum and average
156 amplitudes) from the damaged zone of the Gubbio normal fault zone in central Italy. They
157 showed that the amount of contractional strain accommodated by stylolites as well as their
158 length and their number increase according to the topography parameters. Analyses of
159 cores from boreholes reveal also an increase in stylolite abundance with depth [Lind,
160 1993]. Fabricius and Borre [2007] compared formations of chalk from boreholes on the
161 Ontong Java Plateau and in the central North Sea. They showed that the burial stress
162 and the temperature play distinct roles in the burial diagenesis and porosity development
163 of chalk. Pressure-solution and physical compaction are controled by the burial stress
164 while the temperature controls recrystallization and cementation. Moreover, Lind [1993]
165 suggests that mineralogical anomaly is an initializing factor in stylolite formation such as
166 burrows, shale clasts or flaser structures. Many studies were conducted on the morphology
167 of sedimentary stylolites [Renard et al., 2004; Brouste et al., 2007; Ebner et al., 2009b].
168 Morphology analyses can be done on 1D profiles or 2D opened surfaces. They consist

on studying a stylolitic profile or surface height variations (standard deviation, height differences, power spectrum, average wavelet coefficient spectrum, etc.) over different scales [Schmittbuhl *et al.*, 1995, 2004; Renard *et al.*, 2004]. These analyses reveal two distinct scaling regimes that could be described by power laws. The power laws are function of a roughness exponent also called Hurst exponent inferred to be 1 and 0.5 for small and large scale respectively [Renard *et al.*, 2004; Schmittbuhl *et al.*, 2004; Brouste *et al.*, 2007; Ebner *et al.*, 2009b]. The two regimes are separated by a cross-over length typically around 1 mm [Renard *et al.*, 2004; Schmittbuhl *et al.*, 2004]. For sedimentary stylolites, the two dimensional (2D) analysis of their surface does not show any significant inplane anisotropy reflecting the fact that horizontal stresses are isotropic. Ebner *et al.* [2010a] observed that the profiles of tectonic stylolites show the same geometric attributes as sedimentary ones. Two different regimes are also observed with Hurst exponent around 1 and 0.5 for small and large scale respectively. However, for tectonic stylolites, the 2D analysis revealed an anisotropy of the cross-over length which varies with the direction in the plane of stylolites. Ebner *et al.* [2010a] argue that this anisotropy develops because the stylolite roughens in an anisotropic inplane stress field. The vertical and inplane horizontal stresses are significantly different. In recent papers, stylolites are presented as fossilized signatures of the stress field [Renard *et al.*, 2004; Schmittbuhl *et al.*, 2004; Ebner *et al.*, 2009b, 2010a]. The existence of two scaling regimes for sedimentary stylolites was shown in Schmittbuhl *et al.* [2004] where a brief theoretical derivation was performed. It was shown that the cross-over length between both scaling regimes is expected to be dependent on the stress acting on the stylolite during its growth. Their conclusion was that stylolite morphology can be used as a paleostress magnitude indicator. This

192 conclusion was later probed independently on two types of approaches: first, on field data
193 sampled from the same formation at different heights, *Ebner et al.* [2009b] showed that the
194 measured cross-over length in the morphology followed the expected scaling with the burial
195 stress, evaluated from the position in the formation. Next, discrete numerical simulations
196 were carried out at different stress magnitudes, allowing for the dissolution of grains along
197 the fluid/rock interface, with free energy depending on interfacial tension and local stress.
198 It was shown that the two expected scaling regimes were observed [*Koehn et al.*, 2007;
199 *Koehn*, 2012], and that the cross-over length followed the predicted dependence on the
200 far-field stress amplitude [*Koehn*, 2012].

201 Interfaces between solids and fluids are related to models of stylolitization. In the case
202 where a solid in contact with a fluid is stressed, an instability due to pressure-solution
203 was shown theoretically to exist and is called the Asaro-Tiller-Grinfeld (ATG) instability
204 [*Renard et al.*, 2004]. In models of dissolving surfaces with a stress imposed to a solid in
205 contact with a fluid at chemical equilibrium, this instability leads to the growth of initial
206 large scale modulations of the surface with a wavelength selection obtained through a
207 fastest growing mode. The basic equation depends on the particular boundary conditions
208 e.g. when two solids with different elastic properties are in contact and submitted to a
209 stress, the interface can undergo a fingering instability led by the contrast between the
210 free energies applied to both solids [*Angheluta et al.*, 2008, 2009, 2010]. The stability
211 analysis can be performed theoretically from expressions for the kinetics using local free
212 energy criteria for the reaction rate [*Renard et al.*, 2004; *Schmittbuhl et al.*, 2004], or
213 global ones [*Bonnetier et al.*, 2009; *Angheluta et al.*, 2008]. Depending on the boundary
214 conditions, this situation is also found to be unstable for perturbations exceeding a certain

215 wavelength, leading to fingering (as e.g. with large stress tangential to a fluid interface,
216 or a stress normal to fluid interfaces and lateral periodic boundary conditions [*Bonnetier*
217 *et al.*, 2009]). With other boundary conditions, the surface energy and elastic interactions
218 are found to stabilize the interfaces, which are only destabilized by material noise due to
219 heterogeneities [*Schmittbuhl et al.*, 2004; *Koehn et al.*, 2007]. We will argue in details in the
220 discussion section about the different possibilities applied to the geometry of stylolites,
221 and the fact that stylolites displaying self-affine scaling laws for their height at large
222 scale are compatible with the stabilizing character of elastic forces at large scale. This
223 manuscript provides the technical development and details that lead to the final result
224 that was previously published without derivation, in a condensed form [*Schmittbuhl et al.*,
225 2004]. It also compares the result of the analytical development to a direct numerical
226 simulation.

227 In this paper we concentrate on the following questions: (i) Is the elastic energy sta-
228 bilizing or destabilizing? (ii) What is the significance of the obtained paleostress values?
229 To answer to these questions, (i) we derive the details of the computation leading to the
230 link between the paleostress magnitude and the cross-over length between the two scaling
231 regimes. This is performed by a perturbative analysis of the elastic energy around an
232 interface slightly wavy and unaligned with one of the principal stresses. Then we show in
233 details that the mechanics and chemistry allow to relate the small and large scale behavior
234 of stylolites to known models, with Hurst exponents corresponding to the observed ones.
235 (ii) We finally present and discuss an application in relation with the geological context.
236 This is made on a stylolite from the Bure carbonates and it shows how the predicted

scaling regimes can be found, and how to determinate the paleostress from the extracted cross-over length.

2. Analytical approach : Continuous elastostatic model for stylolite propagation

The rough morphology of stylolites arises from the disorder present in a rock and its impact on the pressure-solution process. This disorder is spatially linked to the grains constituting the rock. To understand the impact of this disorder on the chemico-mechanical coupling, we will consider the following simplified geometry: the initial stage of the stylolite is modeled as an elongated fluid pocket enclosed between two contactless rough surfaces of infinite extent. The contacts between these two surfaces can in principle modify the geometry of the resulting dissolution surface. However, they are assumed to be sufficiently loose in a stylolite and thus the main morphological results are not affected. This assumption simplifies the problem since the dissolution process, happening on both sides of the stylolite (Figure 1), can be described as the dissolution of a solid half-plane in contact with a fluid. With this geometry, the small and large scale self-affine behaviors of the dissolution surface and the associated roughness exponents (or Hurst exponents) are well reproduced. The model leads to the characteristic exponents typically observed in previous studies [Renard *et al.*, 2004; Schmittbuhl *et al.*, 2004; Brouste *et al.*, 2007; Ebner *et al.*, 2009b].

The average stylolitic plane is defined along the x and y -axis (Figure 2). To have better statistics on the morphology of the studied surfaces, the model is assumed to be invariant by translation along the y -axis. It allows to us to describe a larger range of scales at the same numerical cost and to numerically solve the self-affine behavior of the

resulting pressure-solution surface over a larger number of orders of length scales. The same approach can be considered using invariance by translation along the x -axis. In the model we assume a mechanical equilibrium throughout the system and express the dissolution rate as a function of the stress tensor and of the area of interface per unit volume.

2.1. Force perturbation related to the mechanical equilibrium along the fluid-solid interface

First, we express the mechanical equilibrium at the solid-fluid interface (Figure 2). The convention adopted is that compressive stresses and compactive strains are negative *Landau and Lifchitz* [1986]. The far-field stress applied to the host rock is denoted by $\bar{\sigma}^0$. The largest principal stress axis, perpendicular to the average plane of the stylolite, is defined along the z -axis. The fluid pocket transmits all the load through itself (The boundary condition of the fluid pocket is approximated as undrained for that respect: if there is any flow, from or into the fluid pocket, it happens slowly, via the lateral ends. If there is any contact between the opposite walls perpendicular to the main fluid direction, the load transmitted through this contact is neglected). The fluid pressure is thus homogeneous and equal to the largest principal stress applied to the host rock, considering the integral of the local stress field $\bar{\sigma}$ along an elongated rectangular boundary (dashed line in Figure 1):

$$p = -\sigma_{zz}^0 \quad (1)$$

Locally, the local stress $\bar{\sigma}$ is split between the far-field asymptotic value $\bar{\sigma}^0$ and a perturbation generated by the irregular nature of the interface $\bar{\sigma}^1$:

$$\bar{\sigma}(x) = \bar{\sigma}^0 + \bar{\sigma}^1(x) \quad (2)$$

The far-field stress unit vectors \hat{x} and \hat{z} along the x and z -axis are assumed to be the principal directions i.e.

$$\bar{\sigma}^0 = \sigma_{xx}^0 \hat{x}\hat{x} + \sigma_{zz}^0 \hat{z}\hat{z} \quad (3)$$

Here, the notations $\hat{x}\hat{x}$ and $\hat{z}\hat{z}$ correspond to unit matrixes composed from the unit vectors, as e.g. are $\hat{y}\hat{y}$, $\hat{x}\hat{y}$, or $\hat{z}\hat{x}$. This canonical basis for the matrixes is composed from the doublets of unit vectors \hat{x}, \hat{y} and \hat{z} . For example, $\hat{x}\hat{z}$ represents the unit matrix with all components equal to zero, apart from a unit in the lign corresponding to the x coordinate, and the column corresponding to the z one, so that for a pair of vectors u, v applied to the left and right of this matrix, $u \cdot (\hat{x}\hat{z}) \cdot v = (u \cdot \hat{x})(\hat{z} \cdot v) = u_x v_z$. In other terms, with cartesian components along directions of indexes i and j , and the help of the Kronecker symbol δ , the components of the matrix $\hat{x}\hat{z}$, for example, are: $(\hat{x}\hat{z})_{ij} = \delta_{ix}\delta_{jz}$. This convention to define the canonical basis of matrix space (nine elementary second order dyadic products like $\hat{x}\hat{z}$) from the three basic unitary vectors of the vectorial space, \hat{x}, \hat{y} and \hat{z} is, for example, defined by [Gonzalez and Stuart, 2008].

For a stylolite, the largest compressive stress axis is normal to its average plane and thus to the average fluid pocket direction:

$$|\sigma_{zz}^0| > |\sigma_{xx}^0| \quad (4)$$

This relation has strong implications on the stability of the surface pattern emerging from the dissolution process. The far-field deviatoric stress is defined as:

$$\sigma_s^0 = (|\sigma_{zz}^0| - |\sigma_{xx}^0|) = (\sigma_{xx}^0 - \sigma_{zz}^0) \quad (5)$$

To express the force perturbation related to the curved nature of the interface, we define the unit vector \hat{n} normal to the surface pointing towards the fluid. This vector is assumed

to be close to the principal stress axis. In the following, we will consider small-angle deviations from a straight surface, and the results will therefore be valid for small surface slopes only. The model presented below aims to describe the onset of the stylolite propagation from a flat surface, and it will also describe the evolution of large wavelength modes, if the aspect ratio of such modes (ratio of the amplitude over the wavelength) stays small, corresponding to small effective slopes at large wavelength.

The interface is described as a single-valued function $z(x)$ and the slopes are assumed to be of the order ϵ i.e. that $|\partial_x(z)| \in O(\epsilon) \ll 1$. Since the normal \hat{n} to the interface of slope $\partial_x z$ can be expressed by the conditions of normality to the interface, $\hat{n} \cdot (1, \partial_x z)^T = 0$ (at any order of ϵ), and by its unitary norm $\hat{n}^2 = 1$, it is in general $\hat{n} = (-(\partial_x z)\hat{x} + \hat{z})/\sqrt{1 + (\partial_x z)^2}$. Using the above limit of small slopes, developing in ϵ , we obtain to leading order

$$\hat{n} = \hat{z} - (\partial_x z)\hat{x} + O(\epsilon^2) \quad (6)$$

(The order $O(\epsilon)$ is absent from \hat{n}).

The local mechanical equilibrium at the solid-fluid interface is expressed as:

$$\sigma \cdot \hat{n} = -p\hat{n} \quad (7)$$

And with equations (1-7) the force perturbation (illustrated in Figure 3) becomes:

$$\begin{aligned} \delta f(x) &= \sigma^1(x) \cdot \hat{n} = \\ &= -p\hat{n} - \sigma^0 \cdot \hat{n} \\ &= \sigma_{zz}^0[\hat{z} - (\partial_x z)\hat{x}] - \sigma_{zz}^0\hat{z} + \sigma_{xx}^0(\partial_x z)\hat{x} \\ &= (\sigma_{xx}^0 - \sigma_{zz}^0)(\partial_x z)\hat{x} \\ &= \sigma_s^0(\partial_x z)\hat{x} \end{aligned} \quad (8)$$

2.2. Chemico-mechanical coupling

Next, we express the chemico-mechanical coupling. The dissolution speed normal to the solid/fluid interface (in $\text{mol} \cdot \text{m}^{-2} \cdot \text{s}^{-1}$), is to the first order proportional to the chemical potential $\Delta\mu$ of the chemical product dissolving [Kassner et al., 2001; Misbah et al., 2004; Schmittbuhl et al., 2004; Koehn et al., 2007]:

$$v = m\Delta\mu \quad (9)$$

where

$$m = k_0\Omega/RT \quad (10)$$

is the mobility of the dissolving species, $R = 8.31 \text{ J} \cdot \text{mol}^{-1} \cdot \text{K}^{-1}$ is the universal gas constant, T is the temperature in Kelvin, k_0 is a dissolution rate which can be measured experimentally, and Ω is a molar volume. For calcite, $\Omega \simeq 4 \cdot 10^{-5} \text{ m}^3 \cdot \text{mol}^{-1}$ and $k_0 \simeq 10^{-4} \text{ mol} \cdot \text{m}^{-2} \cdot \text{s}^{-1}$ for dissolution in water at atmospheric pressure and 298°K [De Giudici, 2002; Schmittbuhl et al., 2004]. The difference in chemical potential from the solid state to the fluid state is [Kassner et al., 2001; Misbah et al., 2004; Koehn et al., 2007]:

$$\Delta\mu = \Delta\Psi_s + \Omega\Delta P_n + \Omega\gamma\kappa \quad (11)$$

Considering a solid state at given pressure and elastic free energy in chemical equilibrium with the fluid, $\Delta\Psi_s$ and ΔP_n are defined respectively as the change in Helmholtz free energy per mole and the change in stress normal to the interface. The last term corresponds to the surface energy with $\kappa = \partial_{xx}z$, the surface curvature (the inverse of the radius curvature) and γ the surface tension between the solid and the fluid phase. In a particular case, neglecting temperature variation effects and assuming that the fluid composition is in chemical equilibrium with a solid flat surface at normal pressure p and stress σ_{ref} , Eq.(11)

344 reduces to :

$$345 \quad \Delta\mu = 0 \quad (12)$$

$$346 \quad \kappa = 0 \quad (13)$$

347 More generally, by definition ([*Kassner et al.*, 2001]):

$$348 \quad \Delta\Psi_s + \Omega\Delta P_n = \Omega\Delta u_e, \quad (14)$$

349 where

$$350 \quad \Delta u_e = u_e(\sigma) - u_e^{ref} \quad (15)$$

351 and

$$352 \quad u_e = [(1 + \nu)\sigma_{ij}\sigma_{ij} - \nu\sigma_{kk}\sigma_{ll}]/4E \quad (16)$$

353 is the elastic free energy per unit volume with E the Young's modulus and ν the Poisson's
354 ratio of the elastic solid [*Kassner et al.*, 2001; *Landau and Lifchitz*, 1986].

355 To take into account the dissolution speed variations associated to the morphology of
356 the stylolite, we develop the dissolution speed to the leading order as:

$$357 \quad v = v^0 + v^1 \quad (17)$$

358 With equations (9-16):

$$\begin{aligned} 359 \quad v^0 &= \frac{k_0\Omega^2}{RT} \left(\frac{[(1 + \nu)\sigma_{ij}^0\sigma_{ij}^0 - \nu\sigma_{kk}^0\sigma_{ll}^0]}{4E} - u_e^{ref} \right) \\ 360 \quad &= \frac{k_0\Omega^2}{RTE} (\alpha p_0^2 - \alpha_{ref} p_{ref}^2) \end{aligned} \quad (18)$$

361 The geometrical factor α is computed assuming $\sigma_{xx}^0 = \sigma_{yy}^0 = -p_0 + \sigma_s/3$ and $\sigma_{zz}^0 =$
362 $-p_0 - 2\sigma_s/3$:

$$363 \quad \alpha = \frac{9(1 - 2\nu) + 2(1 + \nu)\sigma_s^2/p_0^2}{\text{March 31, 2012, 6:14pm}} \quad (19)$$

D R A F T

D R A F T

α_{ref} is expressed with a similar expression and characterizes the chemical equilibrium with the fluid at the referential state as a function of the pressure p_{ref} and the shear stress σ_{ref} . Typically, for a limestone with a Young's modulus $E = 80$ GPa stressed at $p_0 \simeq 10$ MPa (which corresponds to a few hundred of meters deep in sedimentary rocks) and for a fluid with a chemical composition in equilibrium with the solid, the dissolution speed at the solid-fluid interface in a limestone is of the order of:

$$v_n^0 \simeq 10^{-6} \text{ to } 10^{-5} \text{ m.year}^{-1}$$

2.3. Consequences for the stability of the dissolution process

From the local mechanical equilibrium and the nature of the chemico-mechanical coupling, some important considerations can be inferred about the morphological stability of the dissolution surfaces. This behavior depends on the orientation of the surfaces with respect to the far-field stress.

Previously we have shown how to express the force perturbation arising from the mismatch between the solid-fluid interface orientation and the principal axis of the far-field stress tensor \hat{x} (equation 8).

This relationship holds independently of the relative magnitudes of the principal stresses σ_{xx} and σ_{zz} . If the largest principal stress is tangential to the interface, which is not the case for stylolites, $\sigma_s^0 < 0$ and the sign of $\delta f(x) \cdot \hat{x}$ is opposite to the slope of the interface $\partial_x z$. Such tangential force perturbation is concentrated at the points lying ahead of the average dissolution front (Figure 4). The elastic forces concentrate stress at the valleys of the dissolution front where the free energy is thus higher. This leads to an increased dissolution speed at the points lying ahead of the averaged front. The dissolution propagates downwards. The points at the crests, i.e. located behind the averaged dissolution front,

show a reduced rate of dissolution thus pushing them further from the average front. The points lying out of the average dissolution plane tend therefore to depart further from the average position. The elastic force is in this situation a destabilizing force. On the contrary, the surface tension tends to stabilize the process by decreasing the surface area by flattening the interface.

The competition between the elastic long-range destabilizing forces and the surface tension short-range stabilizing forces leads to the ATG interface instability. The fastest growing wavelength is determined by the balance between these long-range destabilizing and short-range stabilizing effects. Such instability arising in stressed solids was studied theoretically [*Asaro and Tiller*, 1972; *Grinfeld*, 1986; *Misbah et al.*, 2004] and observed experimentally in stressed soluble crystals immersed in a saturated fluid [*Den Brok and Morel*, 2001; *Koehn et al.*, 2004].

If the largest principal stress lies perpendicular to the interface, as for stylolites, $\sigma_s^0 > 0$ and the sign of $\delta f(x) \cdot \hat{x}$ is the same as the slope of the interface $\partial_x z$. Such tangential force perturbation is concentrated at the points lying behind of the average dissolution front (Figure 5). The elastic forces concentrate stress at the crests of the dissolution front where the free energy is thus higher. This leads to an increased dissolution speed for the points lying behind the averaged front. The dissolution propagates downwards. The points at the valleys, i.e. located ahead of the averaged dissolution front, tend to come back to the average position. The elastic force is a stabilizing force in this situation. Here, the surface tension is again a stabilizing process.

Since the long-range elastic force and the short-range surface tension force are stabilizing forces, if the modeled solid properties are purely homogeneous (i.e. homogeneous elastic

solid with homogeneous dissolution rate properties), the model predicts the flattening of any initial non-plane surface with time.

Consequently, to model the morphogenesis of stylolites, which are rough surfaces, we will take here into account the disorder linked to the material properties.

2.3.1. Consequence on initial evolution of trapped fluid pocket

In summary, the above arguments show that an elementary bump of a flat surface disappears for $\sigma_s > 0$, or grows for $\sigma_s < 0$. Qualitatively, if the argument on the stability of surfaces depending on their orientation on the principal stress axis extends for more local orientations along trapped fluid pockets, one should observe the following: for the sides of a fluid pocket lying tangentially to the largest stress, these should develop instable grooves penetrating into the solid, similarly to the ATG instability case. On the contrary, the sides normal to the largest stress direction should remain relatively flat, apart from the fluctuations due to the disorder. These small variations along the surfaces normal to the principal stress axis, and the penetrations of grooves of characteristic wavelength in the rock along the direction of the weakest stress, should lead to the development of elongated structures, and merge initially separated fluid pockets (or clay-enriched pockets). This qualitative mechanism is illustrated on Figure 6. This expectation of qualitative evolution is indeed compatible with the mechanism of development of anti-cracks numerically obtained by *Koehn et al.* [2003]. The experimental grooves observed along the free surface on the sides of a fluid-filled cylindrical pocket by *Den Brok and Morel* [2001] also displayed this trend.

2.4. Expression of the dissolution speed perturbation as a function of the interface shape

To model the disorder in the solid we assume that the material properties (related to the solid grains) vary in a random and spatially uncorrelated way. This disorder can originate from the diversity of grain composition, grain size or orientation, i.e. it represents the small scale heterogeneities present in the rock. For example, the dissolution rate k can be expressed as an averaged term k_0 plus some spatial variations of zero average $\eta(x, z) \cdot k_0$:

$$k = k_0(1 + \eta(x, z(x))) \quad (20)$$

The random variable η is a quenched disorder with no spatial correlations and is characterized by its mean $\langle \eta \rangle = 0$ and its variance $\langle \eta^2 \rangle$ assumed to be small enough to keep small local slopes. The dynamics of the dissolving interface $z(x, t)$ can be expressed from equations (9-17) as:

$$\begin{aligned} v = -\partial_t z &= \frac{k\Omega^2}{RT}(\Delta u_e + \gamma\partial_{xx}z), \\ &= \frac{k_0\Omega^2}{RT}(1 + \eta)\{(1 + \nu)[(\sigma_{ij}^0 + \sigma_{ij}^1)(\sigma_{ij}^0 + \sigma_{ij}^1) - \nu(\sigma_{kk}^0 + \sigma_{kk}^1)^2]/4E - u_{ref}^e + \gamma\partial_{xx}z\} \\ &= \frac{k_0\Omega^2}{RT}\{(1 + \nu)[\sigma_{ij}^0\sigma_{ij}^0 - \nu(\sigma_{kk}^0)^2]/4E - u_{ref}^e\} \\ &+ \frac{k_0\Omega^2}{RT}\eta\{(1 + \nu)[\sigma_{ij}^0\sigma_{ij}^1 - \nu(\sigma_{kk}^0)^2]/4E - u_{ref}^e\} \\ &+ \frac{k_0\Omega^2}{RT}\{(1 + \nu)[2\sigma_{ij}^0\sigma_{ij}^1 - 2\nu(\sigma_{kk}^0\sigma_{kk}^1)]/4E + \gamma\partial_{xx}z\} \end{aligned} \quad (21)$$

i.e., using Eq.(18) for the expression of $\sigma_{ij}^0\sigma_{ij}^0 - \nu(\sigma_{kk}^0)^2$, a dissolution speed separated between an average homogeneous speed v_0 and a leading order of the perturbations v_1 , first order in ϵ as

$$\partial_t z(x, t) = -v_0 - v_1(x, t) \quad (22)$$

with v_0 the dissolution speed given by equation (18) and v_1 a deviation of the dissolution speed with respect to the average dissolution speed v_0 expressed as:

$$v^1 = \frac{k_0 \Omega^2 (\alpha p_0^2 - \alpha_{ref} p_{ref}^2)}{RT E} \eta(x, z(x)) + \frac{k_0 \Omega^2}{RT} \gamma \partial_{xx} z(x) + \frac{k_0 \Omega^2}{RT} \left(\frac{[(1 + \nu) \sigma_{ij}^0 \sigma_{ij}^1 - \nu \sigma_{kk}^0 \sigma_{ll}^1]}{2E} \right) \quad (23)$$

σ^1 is the stress perturbation mentioned previously in equation (2). It is generated by the surface distribution of the tangential force perturbation $\delta f(x)$ due to the irregular nature of the interface.

The first term is a quenched disorder term leading to the roughening of the interface. The second one is a stabilizing quadratic short-range term arising from the surface tension. The last term can be expressed via a non-local kernel from the shape of the interface $z(x)$ by integrating the elastostatic equations in the solid half-plane.

2.5. Detailed form of the elastic long-range interaction kernel

The stress perturbation induced by the force perturbation $\delta f(x)$ (equation 8) exerted on the surface can be determined via the Green function method. Following *Landau and Lifchitz* [1986], the displacement induced by an elementary force \hat{x} applied at the origin $(0, 0, 0)$ on a semi-infinite solid is:

$$\begin{aligned} a_x(x, y, z) &= \frac{1 + \nu}{2\pi E} \left\{ \frac{2(1 - \nu)r + z}{r(r + z)} + \frac{(2r(\nu r + z) + z^2)}{r^3(r + z)^2} x^2 \right\} \\ a_y(x, y, z) &= \frac{1 + \nu}{2\pi E} \left\{ \frac{2r(\nu r + z) + z^2}{r^3(r + z)^2} xy \right\} \\ a_z(x, y, z) &= \frac{1 + \nu}{2\pi E} \left\{ \frac{(1 - 2\nu)x}{r(r + z)} + \frac{zx}{r^3} \right\} \end{aligned} \quad (24)$$

468 where r is the distance relatively to the force application point at $(0, 0, 0)$, i.e. $r^2 =$
 469 $x^2 + y^2 + z^2$. The associated strain applied on the solid is:

$$470 \quad \epsilon_{ij}^e = \frac{1}{2}(\partial_i a_j + \partial_j a_i) \quad (25)$$

471 and the associated stress is:

$$472 \quad f_{ij}(x, y, z) = \frac{E}{1 + \nu}(\epsilon_{ij}^e + \frac{\nu}{1 - 2\nu}\epsilon_{kk}^e\delta_{ij}) \quad (26)$$

473 The stress associated to the point force \hat{x} applied on the surface of normal \hat{z} at the origin
 474 is equal at the origin itself to $\hat{x}\hat{z} + \hat{z}\hat{x}$.

Since the model treated here is invariant by translation along y , the force perturbation $\delta f(u) = \sigma_s^0(\partial_u z)(u)\hat{x}$ is exerted at any $v \in]-\infty, \infty[$ and the resulting displacement field at (x, y, z) , is solely dependent on (x, z) and can be expressed, by linearity of the elastostatics equations, (similarly to the elastostatic Green function method detailed in Eq.(8.14) by [Landau and Lifchitz, 1986]), as a displacement field w of components

$$w_i(x, y = 0, z) = \int_{u=-\infty}^{\infty} \int_{v=-\infty}^{\infty} a_i(x - u, -v, z) du dv \delta f(u) . \hat{x} \quad (27)$$

The associated strain perturbation is

$$\epsilon_{ij}^p = \frac{1}{2}(\partial_i w_j + \partial_j w_i), \quad (28)$$

and the associated stress,

$$\sigma_{ij}^1(x) = \frac{E}{1 + \nu}(\epsilon_{ij}^p + \frac{\nu}{1 - 2\nu}\epsilon_{kk}^p\delta_{ij}) + \delta f(x)(\delta_{ix}\delta_{jz} + \delta_{iz}\delta_{jx})\delta(z), \quad (29)$$

where the first term represents the stress induced by the elastic deformation, and the second one the direct application of the force perturbation on the surface. In the above, the spatial derivative of Eq.(28) can be exchanged with the integration in Eq.(27), to

obtain

$$\epsilon_{ij}^p(x, y=0, z) = \int_{u=-\infty}^{\infty} \int_{v=-\infty}^{\infty} \epsilon_{ij}^e(x-u, -v, z) du dv \delta f(u) \cdot \hat{x}. \quad (30)$$

Recalling the expression of the force perturbation, Eq.(8), from Eq.(29), the stress perturbation along the surface, at $z=0$, is thus:

$$\begin{aligned} \sigma_{ij}^1(x) &= \sigma_s^0 \cdot p.p. \left[\int_{u=-\infty}^{\infty} du (\partial_u z)(u) \right. \\ &\quad \left. * \int_{v=-\infty}^{\infty} f_{ij}(x-u, -v, 0) dv \right] \\ &\quad + \sigma_s^0 (\partial_x z)(x) (\delta_{ix} \delta_{jz} + \delta_{iz} \delta_{jx}) \end{aligned} \quad (31)$$

where p.p. refers to the principal part of the integral. Taking the derivatives of the displacement field (equation 25), we can calculate the associated stress. Integrating this result along the y -axis gives:

$$\int_{v=-\infty}^{\infty} f_{ij}(x, -v, 0) dv = -\frac{2\nu}{\pi x} (\delta_{ix} \delta_{jx} + \delta_{iy} \delta_{jy}) \quad (32)$$

and thus,

$$\begin{aligned} \sigma^1(x) &= -\frac{2\nu\sigma_s^0}{\pi} \cdot p.p. \left[\int_{x'=-\infty}^{\infty} du \frac{(\partial_u z)(u)}{x-u} \right] (\hat{x}\hat{x} + \hat{y}\hat{y}) \\ &\quad + \sigma_s^0 \cdot (\partial_x z)(x) (\hat{x}\hat{z} + \hat{z}\hat{x}) \end{aligned} \quad (33)$$

The elastic energy perturbation associated to the interface deformation can be computed using equation (33) and the relation:

$$\sigma^0 = -(p_0 - \sigma_s^0/3)(\hat{x}\hat{x} + \hat{y}\hat{y}) - (p_0 + 2\sigma_s^0/3)\hat{z}\hat{z} \quad (34)$$

It results in:

$$\begin{aligned} u_e^1 &= \frac{[(1+\nu)\sigma_{ij}^0\sigma_{ij}^1 - \nu\sigma_{kk}^0\sigma_{ll}^1]}{2E} \\ &= \frac{2\nu[(1-2\nu)p_0]}{\pi E} * \sigma_s^0 \cdot p.p. \left[\int_{u=-\infty}^{\infty} du \frac{(\partial_u z)(u)}{x-u} \right] \end{aligned} \quad (35)$$

2.6. Dynamic equation for the dissolution interface

The equation (22) rules the dynamics of the interface dissolution. When computed with equation (18), it gives:

$$\begin{aligned} \frac{RT}{k_0\Omega^2}v^1 &= \frac{(\alpha p_0^2 - \alpha_{ref}p_{ref}^2)}{E}\eta(x, z(x)) \\ &\quad - \gamma\partial_{xx}z(x) \\ &\quad + \beta\frac{p_0\sigma_s^0}{E} \cdot p.p. \left[\int_{u=-\infty}^{\infty} du \frac{(\partial_u z)(u)}{x-u} \right] \end{aligned} \quad (36)$$

where β is a geometrical factor:

$$\beta = [2\nu(1 - 2\nu)]/\pi \quad (37)$$

Equation (23) can be expressed in a dimensionless form by using length and time units as:

$$L^* = \gamma E / (\beta p_0 \sigma_s) \quad (38)$$

$$\tau = (L^*)^2 RT / (\gamma k_0 \Omega^2) \quad (39)$$

We define the dimensionless variables in the reference frame moving at the average velocity $-v_0$ as:

$$z' = [z + (v_0 t)] / L^* \quad (40)$$

$$x' = x / L^* \quad (41)$$

$$t' = t / \tau \quad (42)$$

and the reduced quenched noise as:

$$\begin{aligned} \eta'(x', z'(x, t) - v_0 t / L^*) = \\ [(\alpha p_0^2 - \alpha_{ref} p_{ref}^2) / (\beta p_0 \sigma_s)] \eta(x, z(x, t)) \end{aligned} \quad (43)$$

512 The dimensionless stochastic equation for the stylolite growth process is then:

$$\begin{aligned}
513 \quad & \partial_{t'} z'(x', t') = \\
514 \quad & \eta'(x', z'(x', t') - v_0 \tau t' / L^*) + \partial_{x' x'} z' \\
515 \quad & - p.p. \left[\int_{u=-\infty}^{\infty} du \frac{(\partial_u z')(u)}{x' - u} \right]
\end{aligned} \tag{44}$$

516 At large average dissolution speed, the term $v_0 \tau t' / L^*$ takes over z quickly and the noise
517 is annealed, becoming mostly time-dependent. On the contrary, for sufficiently slow pro-
518 cesses such as the extend of the surface roughness over several grains, the noise can be
519 considered as quenched. This is the case here as the changes in η' arising from $z(x, t)$
520 are significantly larger than the changes due to some variations of the average dissolution
521 front position $v_0 \tau t' / L^*$. To the first order, the noise dependence is mainly $\eta'(x', z'(x', t'))$
522 and the noise will therefore be considered here as quenched.

523 The dynamic equation then becomes:

$$\begin{aligned}
524 \quad & \partial_{t'} z'(x', t') = \eta'(x', z'(x', t')) + \partial_{x' x'} z' \\
525 \quad & - p.p. \left[\int_{u=-\infty}^{\infty} du \frac{(\partial_u z')(u)}{x' - u} \right]
\end{aligned} \tag{45}$$

526 Alternatively, in some arbitrary spatial unit ℓ , this can also be written:

$$527 \quad \partial_t z(x, t) = \eta''(x', z'(x', t')) + \partial_{xx} z - \frac{\ell}{L^*} \int dy \frac{\partial_y z}{x - y} \tag{46}$$

528 with $L^* = \gamma E / (\beta p_0 \sigma_s)$ and $\tau = \ell^2 R T / (\gamma k_0 \Omega^2)$, the time unit.

2.7. Small and large scale behavior of the model

529 Elastic interactions can be neglected in equation (46) for small scales such as $\ell \ll L^*$
530 (the lower limit corresponds to the resolution of the analyzed signal) reducing the model

to a Laplacian description:

$$\partial_t z'(x, t) = \partial_{xx} z' + \eta(x, z'(x)) \quad (47)$$

This equation is known as the Edwards Wilkinson model [Edwards and Wilkinson, 1982] modified with a quenched random noise. It has been studied in the literature and leads to the growth of self-affine surfaces of roughness $\zeta \sim 1.2$ [Roux and Hansen, 1994], in agreement with existing data on stylolites where $\zeta \sim 1.1$ [Schmittbuhl et al., 2004].

Conversely, for large scales $\ell \gg L^*$ (the upper limit corresponds to the system size), surface tension can be neglected reducing equation (46) to a mechanical regime:

$$\partial_t z'(x, t) = -\frac{\ell}{L^*} \int dy \frac{\partial_y z}{x - y} + \eta(x, z'(x)) \quad (48)$$

In this case, the model is similar to known models describing the propagation of an elastic line on a disordered pinning landscape or the propagation of a mode I fracture front in a disordered solid. It leads to the growth of self-affine surfaces of roughness $\zeta \simeq 0.5$ [Tanguy et al., 1998]. In summary, the model derived above predicts the growth of dissolution surfaces with different self-affine characteristics at small scale ($\zeta_1 \sim 1.2$) and large scale ($\zeta_2 \sim 0.5$). The transition between these regimes is expected to occur at a certain cross-over length L^* .

3. Numerical approach : Dynamic evolution of the interface

From a purely analytical point of view and via the similarity of asymptotic form of the dynamic equation with known models for large and small scales, we have shown that two different scaling laws are expected for small and large scales, and that the cross-over length should depend on the far-field stress magnitude. Independently from this general analytical analysis, we will now show how to solve the problem numerically, i.e. implement

the dynamic evolution of the interface with all the large and small scale terms and random variables to represent the disorder and analyse the resulting morphogenesis.

3.1. Practical implementation of the model

We simulate the dissolution process for a calcite-water interface. This is done in an event-driven discrete lattice code, with algorithms corresponding to a discrete Langevin equation leading to grains getting dissolved one at a time: for each grain along the interface, a time to dissolution is computed from the above Langevin equation, and the grain with the shortest dissolution time is removed. After what, the times are recomputed for all grains along the interface, and the next grain with shortest dissolution time is removed, and so on (see *Renard et al.* [2004] for details of the practical implementation). The selected constants correspond to a calcite-water system, $\gamma = 0.27 J \cdot m^{-2}$, $\Omega = 4 \cdot 10^{-5} m^3 \cdot mol^{-1}$, $\nu = 0.25$, $E = 80$ GPa and $k_0 = 10^{-4} mol \cdot m^{-2} \cdot s^{-1}$ [*Renard et al.*, 2004]. The chosen physical conditions are $T = 420$ K, $\langle p \rangle = 10$ MPa and $\langle \sigma_s \rangle = 40$ MPa. The amount of quenched noise is associated to the natural variations of grain properties. The typical scale associated to the quenched disorder (or typical grain size) is considered here to be around $\ell = 10 \mu m$, with no correlation above this scale. This quenched disorder has a standard deviation $\sqrt{\langle \eta^2 \rangle} = [\alpha \ell p_0 / (\beta L^* \sigma_s)] \cdot [(\delta E/E) + (\delta k/k_0) + (\delta \alpha/\alpha)]$ corresponding to some relative variations of the dissolution rate of around 10% (i.e. $\delta k/k_0 \sim 0.1$).

The dimensionless surface dynamic equation without disorder is:

$$\partial_t z(x, t) = v_0 + \partial_{xx} z - \frac{\ell}{L^*} \int dy \frac{\partial_y z}{x - y} \quad (49)$$

where $L^* = \gamma E / (\beta p_0 \sigma_s)$, ℓ is the unit length, and $\tau = \ell^2 R T / (\gamma k \Omega^2)$ is the time unit.

573 We assume a small disorder in the implied quantities (e.g. Young's modulus), that are
574 quenched in the material properties of the rock heterogeneity associated with micrometric
575 grains, typically $\ell = 10\mu\text{m}$. The interface is supposed to be normal to the largest stress
576 direction (stabilizing elastic interactions).

577 Considering a perturbation to the first order, in the referential frame of the homo-
578 geneously moving average front, $z' = z - v_0 t$, the equation ruling the surface growth
579 becomes:

$$580 \quad \partial_t z'(x, t) = \partial_{xx} z - \frac{\ell}{L^*} \int dy \frac{\partial_y z}{x - y} + \eta(x, z(x)) \quad (50)$$

581 with a quenched random term $\eta(x, z'(x)) = [\alpha \ell p_0 / (\beta L^* \sigma_s)] \cdot [(\delta E/E) + (\delta k/k) - (\delta \alpha/\alpha)]$

582 The first and second terms are stabilizing terms. The third term referring to the quenched
583 disorder destabilizes the interface. We perform the simulation of this dynamic equation
584 with both stabilizing terms and quenched noise.

585 The prefactors in equation 50 depend on the rock type and on the applied stress. In
586 addition to these mappings, the characteristic units are known as function of the rock
587 properties. The cross-over scale $L^* = \gamma E / (\beta p_0 \sigma_s)$ is function of the pressure during the
588 growth, through p_0 and σ_s .

589 Determining the cross-over length L^* for natural samples allows to determine such stress
590 value during the growth, and consequently the depth of the rock during the stylolite
591 propagation. Assuming as an order of magnitude $p_0 \sim \sigma_s$ and typical values for the
592 limestone elastic properties and the water calcite reaction rates, $L^* \sim 1\text{mm}$ leads to
593 a typical depth of 1 km. **Stylolites** can thus be considered as **fossils of the stress**
594 **magnitude**.

595 We solved the dynamic equation (46) with an event-driven algorithm where the fastest
596 dissolving grain is removed at each step. The problem is considered as L -periodic and the
597 long-range elastic kernel $p.p. \int dy \frac{\partial_y z}{x-y} = -p.p. \int dy \frac{z(x)-z(y)}{(x-y)^2}$ is replaced by its finite-size form
598 $-p.p. \int_0^L dy \frac{z(x)-z(y)}{\sin^2(\pi(x-y)/L)} \frac{\pi^2}{L^2}$. This standard form can be obtained by solving the elastostatic
599 equations in the Fourier space and performing an inverse Fourier integration. When a new
600 grain is reached, the realization of its quenched disorder η is evaluated using a Gaussian
601 distribution. For the dissolution surface simulated which is 4096ℓ long, 8000000 grains
602 were dissolved.

3.2. Analysis of the small-scale and large-scale roughness of the saturated interface

603 The simulation of the calcite-water system leads to the growth of a dissolution interface.
604 Starting from a flat interface and after a certain transient time, the Fourier modes saturate
605 to a characteristic amplitude. A snapshot of the developed stylolitic interface is shown in
606 Figure 7.

607 This interface fluctuates around the average progressing flat dissolution front. The
608 Fourier power spectrum $P(k, t) = \|\tilde{z}(k, t)\|^2$ of each front $z(x, t)$ is extracted, and the
609 ensemble average of this power spectrum $P(k) = \langle \|\tilde{z}(k)\|^2 \rangle$ is obtained for developed in-
610 terfaces, by averaging over all fronts after 80000 grains have been dissolved. The expected
611 small and large scale self-affine characteristics correspond to the theoretical predictions,
612 as shown in Figure 8. Indeed, the power-spectrum is a power-law of scale, with two dif-
613 ferent exponents at large and small scale, and a cross-over length around the scale L^* :
614 For $k > 2\pi/L^*$ i.e at small scale, we have $P(k) \sim k^{-1-2\zeta}$ with $\zeta_S = 1.2$, and for the large
615 scales, the roughness exponent is found to be around $\zeta_L = 0.35$. The straight lines in the

bilogarithmic axes (Figure 8) correspond to these power law behaviors, determined by
 linear regression over the two domains $k > 2\pi/L^*$ and $k < 2\pi/L^*$. The ensemble used for
 the roughness estimate is the following: it corresponds roughly to 100000 grain being dis-
 solved after the first 80000 first ones, which are discarded. We thus compute the average
 power spectral density profiles over all these states, representative of a saturated situation
 with fluctuations of the Fourier mode amplitude around some characteristic magnitude for
 each wavelength. The linear regression have been performed in bilogarithmic space on
 the ranges $0 < \log_{10}(k) < 1.5$ and $2 < \log_{10}(k) < 3$, with k -unit of $2\pi/L$, with $L = 4096\ell$
 and a grain size $\ell = 10\mu\text{m}$. The standard error bar provided by the linear regression over
 this two ranges is around ± 0.2 in slope (i.e. ± 0.1 for the Hurst exponents ζ).

Thus, we find that the scaling of saturated surfaces in this model is compatible with
 observations made on natural surfaces, and with the previous analytical predictions.

In addition, the dynamic behavior of these models (Edwards Wilkinson in a quenched
 noise [Roux and Hansen, 1994], or elastic string in a disordered landscape [Tanguy et al.,
 1998]) is known. The prefactor (characteristic time) associated with the dynamics can
 be evaluated through the previous computations from the rock material properties. The
 time to saturation at an observation scale of a few centimeters is estimated to be around
 a few thousands of years. The stylolite roughness is hence always in a saturation state for
 a geologist at small observation scale.

However, for longer systems, e.g. decametric ones, much longer times would be required
 for saturation. Such long stylolites are sometimes observed but rarely analyzed in terms
 of scaling of the height. To our knowledge, the only analysis performed on decametric
 size stylolites [Laronne Ben-Itzhak, 2011] showed that these large scale structures were

not saturated. This means that the time during which the stylolitization was active on such very long stylolites was only enough to lead the small scales to saturated amplitude, but not the large ones (above a few tenth of centimeters).

4. Example: Application of the model to natural data

The model is applied to a sedimentary stylolite collected in a core at the Andra (French national radioactive waste management agency) Underground Research Laboratory (URL) at Bure in Eastern France. The selected sample comes from the borehole EST433 at a depth of 720 m. The host rock is a fine-grained, homogeneous grainstone from the Dogger age. The core was cut in three parts thus giving four profiles for analysis (Figure 9).

Profiles 1 and 2 and profiles 3 and 4 are spaced by 3 mm (thickness of the drilling saw) and profiles 2 and 3 are spaced by 30 mm. Each profile has a length around 90 mm. The stylolites were photographed at a resolution of 30 μm . A systematic method was used to extract profiles from the photographs. It consists on isolating the black pixels constituting the clay particles in the stylolite from photographs converted in grey level pictures. The profiles will be used as functions in the spectral analysis (integral transforms) and thus are required to be single-valued. Stylolites show a self-affinity geometry [Schmittbuhl *et al.*, 1995; Barabási and Stanley, 1995] meaning that they are statistically invariant under an affine transformation. Thus, for Δx and Δy the horizontal direction amplitude and Δz the vertical direction amplitude: $\Delta x \rightarrow \lambda \Delta x$, $\Delta y \rightarrow \lambda \Delta y$ and $\Delta z \rightarrow \lambda^\zeta \Delta z$, where λ can take any value and ζ is the Hurst exponent which describes the scaling invariance [Schmittbuhl *et al.*, 2004; Renard *et al.*, 2004]. As in Ebner *et al.* [2009b] we used both the Fourier power spectrum [Schmittbuhl *et al.*, 1995] and the averaged wavelet coefficient [Simonsen *et al.*,

1998] signal processing methods to analyse the profiles (Figure 10). We used two different methods to check the repeatability of the results. First we calculated the Fourier power spectrum $P(k)$, which is the square of the modulus of the Fourier transform, as a function of the wave-number k ($k = 2\pi/L$, where L is the wavelength). The power spectrum expressed as a function of the length for a self-affine profile behaves as $P(L) \simeq L^{2\zeta+1}$. We calculated also the averaged wavelet coefficient spectrum as a function of the scale a with Daubechies 4 wavelets which behaves as $W(a) \simeq a^{1/2+\zeta}$.

The results show the two scaling regimes predicted by the theory presented above, described by two different power laws. Figure 11 shows the Fourier power spectrum for the profile 1 as a function of the length L . The raw data are more concentrated at small scale. The lower limit for the length corresponds to the Nyquist length which is the resolution multiplied by 2. As the profiles have a finite-size the upper limit for the analysis (corresponding to small wave-number) is given by the size of the profile. To analyze the data, we apply a logarithmic binning so that the weight on each point is equal. To estimate the cross-over length, we used a linear-by-part fit with a cross-over function changing the scaling law from small to large scale as explained in *Ebner et al.* [2009b]. The averaged wavelet coefficient spectrum (Figure 12) does not require a binning. The same kind of fitting was used to appraise the cross-over length L^* .

The intersection between both regimes (whose slopes are imposed by $\zeta_S = 1$ and $\zeta_L = 0.5$ for small and large scale respectively) gives the cross-over length L^* . We summarize the estimated cross-over length for all the analyzed profiles with both methods in Table (9). The uncertainties on the cross-over length (68% and 44% for Fourier power spectrum

and averaged wavelet coefficient respectively) are due to the spatial variability of the intersection between the small and large regimes.

5. Discussion

5.1. Interpretations of the estimated paleostress

We discuss three theories about the meaning of the estimated paleostress for the studied sedimentary stylolite:

- Present day stress: if the conditions for pressure-solution (lithostatic pressure in competition with the presence of a fluid at an appropriate state of equilibrium) are present, a stylolite should show the present day state of morphology and is still evolving. This means that we should measure the current applied stress and see the last evolution of the morphology. This can be compared with recent studies where vertical and horizontal stresses were measured in boreholes at Bure [*Wileveau et al.*, 2007; *Gunzburger and Cornet*, 2007] to assess if the estimated stress corresponds to the measured ones.

- Evolution stopped: this can occur if the lithostatic stress becomes too small to encourage the process (change in the magnitude due to a tectonic phase for example). It can also be associated with the closing of the porosity by recrystallization. Indeed, if the pore size decreases because of recrystallization at the pore surface, the surface tension increases preventing more recrystallization. Thus, the water is getting more charged in dissolved materials and the chemistry of the water changes and can stop the stylolite evolution. Moreover, the decrease of the pore size can limit or stop the fluid flow and close the system.

- Reactivation: both previous theories can act on the history of a stylolite. After its initiation, a stylolite can see its growth stopped by the kind of process we developed

just before. If in the geological history an event as emerged soil and/or erosion allows to change the applied stress or to meteoritic fluids to flow in the soil, the system can have its properties changed and pressure-solution process can start again until it is stopped or it can still evolve.

These three theories will be discussed with regard to the paleostress results.

5.2. Estimation of the paleostresses

5.2.1. Hypothesis on the basin evolution

To estimate the paleostress from the model developped in this study, we use the average of the cross-over lengths determined for the four profiles. The cross-over length is related to the stresses by equation (38). However, this equation can be simplified by making assumptions on the surrounding rock formation. We use the same assumptions as in *Ebner et al.* [2009b] for the stylolites from Cirque de Navacelle (Cévennes, France) considering that the initiation of stylolites occurs at the early stage of a basin. The major principal stress is vertical (σ_{zz}) as we analyzed a sedimentary stylolite. The principal horizontal stresses are isotropic ($\sigma_{xx} = \sigma_{yy}$). Thus the mean stress p_0 and the shear stress σ_S are:

$$p_0 = -(2\sigma_{xx} + \sigma_{zz})/3 \quad (51)$$

$$\sigma_S = \sigma_{xx} - \sigma_{zz} \quad (52)$$

As stylolites are known to develop in the early stage of sedimentation of basins, the strain is assumed to be uniaxial:

$$\sigma_{xx} = \sigma_{yy} = \frac{\nu}{1 - \nu} \sigma_{zz} \quad (53)$$

Using equations (51-53), equation (38) becomes:

$$\sigma_{zz}^2 = \frac{\gamma E}{\alpha \beta L^*} \quad (54)$$

725 where

$$726 \quad \alpha = \frac{1(1+\nu)(1-2\nu)}{3(1-\nu)(1-\nu)} \quad (55)$$

727 is a dimensionless geometrical factor. The geometrical factor β (equation 37) is $\beta =$
728 $\nu(1-2\nu)/\pi$. Using the average cross-over length \bar{L}^* in equation (54), we can estimate
729 the main principal paleostress σ_{zz} . The Poisson's ratio ν of the host rock was determined
730 by measuring the P and S elastic wave velocities ($\nu = \frac{0.5(V_P/V_S)^2-1}{((V_P/V_S)^2-1)}$). The relative errors
731 for the measurements of V_P and V_S are 1 and 2% respectively [Benson *et al.*, 2005]. The
732 relative error for the Poisson's ratio is thus equal to 12%. Consequently, α and β have
733 error bars equal to 2% and 22%, respectively. The last constant to be determined is the
734 Young's modulus. The next paragraph details our choices for this matter.

735 5.2.2. Uncertainties on the Young's modulus E

736 In their paper, Ebner *et al.* [2009b] determined E assuming the vertical stress is equal
737 to the lithostatic stress as in equation (56) where z is the current depth of their samples.
738 They plotted the determined stress as a function of $L^{-1/2}$. The slope of the curve is
739 proportional to $E^{1/2}$ (see equation (54)). They found $E = 15$ GPa which is the lowest
740 acceptable limit for limestones [Clark, 1966]. Based on uniaxial loading made in our
741 laboratory, we determined $E = 36.2$ GPa for the rock surrounding the analyzed stylolite.
742 Considering that the limestones from Bure replaced in the geological context of the Paris
743 basin cannot be excessively harder than what we observe today, the value determined in
744 the laboratory is taken as the upper limit for E . Thus we can estimate the paleostress in
745 a small range of E . The values used for the calculation of the paleostress are summarized
746 in Table (5.2.1).

To calculate the paleostress σ_{zz} , we take into account the error bars for each parameter.

The computed error for the calculation of σ_{zz} is 66% for the Fourier power spectrum method and 54% for the averaged wavelet coefficient method. The results are summarized in Table (5.2.2).

5.3. Geological context

By doing some assumptions on the sedimentary overburden, the depth of development of the stylolite can be assessed. The lithostatic pressure σ_{zz} can be expressed as:

$$\sigma_{zz} = \rho gh \quad (56)$$

where ρ is the density in $g \cdot m^{-3}$, g is the Earth's gravity ($g = 9.81 m \cdot s^{-2}$) and h is the depth in m . We make the assumption that at the initiation of the stylolite, linked to the early stage of formation of the sedimentary basin, the overburden was made of limestones only. Thus, we consider the density of limestones $\rho = 2710 g \cdot m^{-3}$. The estimated depths of development of the stylolites are summarized in Figure (12). The error bars on h are of the same order as for the paleostress.

Now we can wonder what is the interpretation of the estimated paleostress with regard to the three theories exposed previously:

1. *Wileveau et al.* [2007] and *Gunzburger and Cornet* [2007] measured the vertical stress at Bure which is equivalent to the lithostatic pressure as in equation (56). Our results show that the calculated depth corresponds to the depth where we cored the analyzed stylolite. Thus the studied stylolite is more likely to be still active and to show the present day stress.

767 2. *André et al.* [2010] discussed about a reactivation of the stylolitization during the

768 Tertiary age (end of Cretaceous more precisely) by the change in the stress orientation

769 or by the emergence of the Cretaceous sediments which were eroded and permitted to

770 meteoritic fluid to spread in the sediments. This reactivation process could have acted on

771 the growth of the studied stylolite until today. But still it seems that the theory of the

772 present day stress is more applicable on that example.

6. Conclusions

773 Analysing the local boundary conditions due to the fact that the inside of a stylolite

774 does not sustain shear stress and an elastic surrounding, we derived the dependence of

775 the free energy along a stylolite surface on the shape of the stylolite. Adding up a surface

776 energy term we derived a dynamic surface evolution model for a stylolitic interface. This

777 model, in the situation where a stylolite is perpendicular to the largest principal stress axis

778 - as in most case - includes terms that lead to the stabilization of the surface dynamics,

779 i.e. to the vanishing of initial perturbations towards a flattening surface. Hence, the

780 presence of disorder linked to the heterogeneities of the material properties is required to

781 explain the rough nature of stylolites. Introducing such non correlated quenched disorder,

782 the model predicts the occurrence of two scaling laws. At small scale, a destabilizing

783 disorder competing with a stabilizing surface energy term give a model similar to the

784 Edwards Wilkinson model in a quenched noise leading to a saturated surface with a Hurst

785 exponent around 1. At large scale, the competition between destabilizing disorder and

786 stabilizing elastic interactions is similar to models of evolution of an elastic interface in

787 quenched disorder leading to a Hurst exponent of 0.5.

788 The cross-over scale between these two scaling regimes was shown to be directly linked
789 to the stress magnitude. Hence, the determination of this cross-over and other physical
790 rock properties allows to use stylolites as markers of the paleostress magnitude.

791 Both scaling laws and the dependence of this cross-over scale on the stress magnitude
792 were derived in two ways: by purely analytical derivation and similarity to known models
793 in section 2 and by numerical integration in section 3.

794 Importantly, it should be noted that the elastic forces, depending on the boundary
795 conditions, can be stabilizing, as here, or destabilizing. The existence of several models
796 and techniques of global or local calculation of the free energy can raise the question
797 of a stabilizing or destabilizing nature of the elastic forces in the context of a stylolite.
798 Independently from the derivation carried out in details in this paper, we note the following
799 argument that can distinguish between stabilizing and destabilizing terms. The only
800 difference between models with stabilizing or destabilizing elastic kernel is the sign of the
801 prefactor in front of the elastic operator in the dynamic equation. However, when this sign
802 is reverted, all large scale wavelength Fourier modes become unstable (with a selection of
803 fastest growing mode, as e.g. shown in *Misbah et al.* [2004] or *Bonnetier et al.* [2009]).
804 Numerical simulations similar to the ones shown above, with a destabilizing mode, do
805 not lead to any saturation of the amplitude of the large modes at long times, and the
806 Fourier power spectrum at a given time does not display any scaling law at fixed time for
807 the large scales. Thus, the scaling laws observed in field stylolites are compatible with a
808 model where elastic forces are stabilizing: we take this as a good sign of validity of the
809 proposed approximations to take the boundary conditions into account in the proposed
810 model.

811 The results from both analytical and numerical independent resolutions presented in
812 this study are also consistent with three other independent observations:

813 • The existence of two Hurst exponents at small and large scales, as observed in *Schmit-*
814 *tbuhl et al.* [2004], in the stylolites from the log cores of Bure (section 4).

815 • The results of recent molecular dynamic models of dissolution with pressure reliance
816 and surface energy terms in the free energy displaying similar scaling laws and an identical
817 law for the dependence of the cross-over length over the applied stress [*Koehn*, 2012].

818 • The model was applied in a previous study to stylolites found at various depths in a
819 limestone formation at Cirques de Navacelles (Cévennes, France). The inferred formation
820 stresses were compatible with the derived weight of overburden at the time of formation
821 [*Ebner et al.*, 2009b].

822 We show finally on the example of sedimentary stylolites in Bure, how the confinement
823 stress can be derived from morphological studies of stylolites. The ubiquitous nature of
824 these pressure-solution features makes them a versatile marker for paleostress magnitude
825 that can give access to the stress during the growth of stylolites. This easily available
826 paleostress marker opens the way for systematic studies of paleostress in large rock for-
827 mations for different stylolite families. However, it must be used carefully as the error
828 bars are not minor. An important number of measurement is required to constrain the
829 results. Together with dating indications for the time of occurrence of such stylolites (as
830 e.g. times of tectonic events) and current stress assessment methods it opens the way for
831 the determination of stress evolution in large basins, which is a key to understand their
832 evolution.

7. Acknowledgments

We would like to thank C. Aurière, J.D. Bernard, T. Reuschlé, A. Steyer, E. Aharonov, Y. Bernabé and J.L. Alves for technical help and discussions. This work was partially funded by the French national radioactive waste management agency (Andra) and supported by a FORPRO grant. The authors would also like to thank the CAPES-COFECUB program for stimulating fruitful discussions.

References

- Aharonov, E., and R. Katsman (2009), Interaction between pressure solution and clays in stylolite development: insights from modeling, *American J. Sci.*, *309*, 607–632.
- André, G. (2003), *Caractérisation des déformations méso-cénozoïques et des circulations de fluides dans l’Est du Bassin de Paris*, Thesis, Université Henri Poincaré, Nancy, France.
- André, G., C. Hirsch, S. Fourcade, M. Cathelineau, and S. Buschaert (2010), Chronology of fracture sealing under a meteoritic fluid environment: microtectonic and isotopic evidence of major Cainozoic events in the eastern Paris Basin (France), *Tectonophysics*, *490*, 214–228.
- Angheluta, L., E. Jettestuen, J. Mathiesen, and F. Renard (2008), Stress-driven phase transformation and the roughening of solid-solid interfaces, *Phys. Rev. Lett.*, (100), 096105.
- Angheluta, L., J. Mathiesen, C. Misbah, and F. Renard (2010), Morphological instabilities of stressed and reactive geological interfaces, *J. Geophys. Res.*, *115*, b06406.

852 Angheluta, L., E. Jettestuen, and J. Mathiesen (2009), Thermodynamics and roughening
 853 of solid-solid interfaces, *Phys. Rev. E*, *79*(3, Part 1), 031601.

854 Asaro, R., and W. Tiller (1972), Interface morphology development during stress-corrosion
 855 cracking. 1. Via surface diffusion, *Met. Trans.*, *3*, 1789.

856 Barabási, A., and H. Stanley (1995), *Fractal concepts in surface growth*, Cambridge Uni-
 857 versity Press.

858 Bathurst, R. G. C. (1971), *Carbonate sediments and their diagenesis*, Elsevier, Amster-
 859 dam/London/New York.

860 Bathurst, R. G. C. (1987), Diagenetically enhanced bedding in argillaceous platform lime-
 861 stones: stratified cementation and selective compaction, *Sedimentology*, *34*, 749–778.

862 Baud, P., E. Klein, and T. F. Wong (2004), Compaction localization in porous sandstones:
 863 spatial evolution of damage and acoustic emission activity, *J. Struct. Geol.*, *26*, 603–624.

864 Benedicto, A., and R. Schultz (2010), Stylolites in limestones: magnitude of contractional
 865 strain accommodated and scaling relationships, *J. Struct. Geol.*, *32*, 1250–1256.

866 Benson, P. M., P. G. Meredith, E. S. Platzman, and R. E. White (2005), Pore fabric
 867 shape anisotropy in porous sandstones and its relation to elastic wave velocity and
 868 permeability anisotropy under hydrostatic pressure, *Int. J. Rock Mech. Min. Sci.*, *42*,
 869 890–899.

870 Bonnetier, E., C. Misbah, F. Renard, R. Toussaint, and J. Gratier (2009), Does roughening
 871 of rock-fluid-rock interfaces emerge from a stress-induced instability?, *European Phys.*
 872 *J. B.*, *67*, 121.

873 Brouste, A., F. Renard, J. P. Gratier, and J. Schmittbuhl (2007), Variety of stylolites’
 874 morphologies and statistical characterization of the amount of heterogeneities in the

875 rock, *J. Struct. Geol.*, *29*, 422–434.

876 Bushinskiy, G. I. (1961), Stylolites, *Izv. Akad. Nauk. SSSR, Ser. Geophys.*, *8*, 31–46.

877 Buxton, T. M., and D. Sibley (1981), Pressure solution features in a shallow buried
878 limestone, *J. Sediment. Petrol.*, *51*, 19–26.

879 Clark, S. P. J. (1966), *Handbook of physical constants*, Geological Society of New-York.

880 Cox, M. A., and J. L. Whitford-Stark (1987), Stylolites in the Caballos Novaculite, West
881 Texas, *Geology*, *15*, 439–442.

882 Cox, S. F., and M. S. Paterson (1991), Experimental dissolution-precipitation creep in
883 quartz aggregates at high temperatures, *Geophys. Res. Lett.*, *18*, 1401–1404.

884 De Giudici, G. (2002), Surface control vs. diffusion control during calcite dissolution:
885 Dependence of step-edge velocity upon solution pH, *American Mineralogist*, *87*(10),
886 1279–1285.

887 Den Brok, S. W. J., and J. Morel (2001), The effect of elastic strain on the microstructure
888 of free surfaces of stressed minerals in contact with an aqueous solution, *Geophys. Res.*
889 *Lett.*, *28*, 603–606.

890 Den Brok, S. W. J., and C. Spiers (1991), Experimental evidence for water weakening
891 of quartzite by microcracking plus solution precipitation creep, *J. Geol. Soc. (London)*,
892 *148*, 541.

893 Dunnington, H. V. (1954), Stylolite development post-dates rock induration, *J. Sediment.*
894 *Petrol.*, *24*, 27–49.

895 Dysthe, D., Y. Podlchikov, F. Renard, J. Feder, and B. Jamtveit (2002), Universal scaling
896 in transient creep, *Phys. Rev. Lett.*, *89*, 246102.

897 Dysthe, D., F. Renard, J. Feder, B. Jamtveit, P. Meakin, and T. Jøssang (2003), High
 898 resolution measurements of pressure solution creep, *Phys. Rev. E*, *68*, 011603.

899 Ebner, M., D. Koehn, R. Toussaint, and F. Renard (2009a), The influence of rock hetero-
 900 geneity on the scaling properties of simulated and natural stylolites, *J. Struct. Geol.*,
 901 *31*, 72–82.

902 Ebner, M., D. Koehn, R. Toussaint, F. Renard, and J. Schmittbuhl (2009b), Stress sen-
 903 sitivity of stylolite morphology, *Earth and Planet. Sci. Lett.*, *277*, 394–398.

904 Ebner, M., R. Toussaint, J. Schmittbuhl, D. Koehn, and P. Bons (2010a), Anisotropic
 905 scaling of tectonic stylolites: a fossilized signature of the stress field, *J. Geophys. Res.*,
 906 *115*, b06403.

907 Ebner, M., S. Piazzolo, F. Renard, and D. Koehn (2010b), Stylolite interfaces and surround-
 908 ing matrix material: Nature and role of heterogeneities in roughness and microstructural
 909 development, *J. Struct. Geol.*, *32*, 1070–1084.

910 Edwards, S. E., and D. R. Wilkinson (1982), The surface statistics of a granular aggregate,
 911 *Proc. R. Soc. London*, *17*.

912 Fabricius, I. L., and M. K. Borre (2007), Stylolites, porosity, depositional texture, and
 913 silicates in chalk facies sediments. Ontong Java Plateau - Gorm and Tyra fields, North
 914 Sea, *Sedimentology*, *54*, 183–205.

915 Fletcher, R. C., and D. D. Pollard (1981), Anticrack model for pressure solution surfaces,
 916 *Geology*, *9*, 419–424.

917 Gonzalez, O., and A. Stuart (2008), *A first course in continuum mechanics*, Cambridge
 918 University Press.

919 Gratier, J. P. (1993), Experimental pressure solution of halite by an indenter technique,
 920 *Geophys. Res. Lett.*, *20*, 1647–1650.

921 Gratier, J. P., and R. Guiguet (1986), Experimental pressure solution-deposition on quartz
 922 grains: the crucial effect of the nature of the fluid, *J. Struct. Geol.*, *8*, 845–856.

923 Gratier, J. P., L. Jenatton, D. Tisserand, and R. Guiguet (2004), Indenter studies of the
 924 swelling, creep and pressure solution of Bure argillite, *App. Clay Sci.*, *26*, 459–472.

925 Gratier, J. P., L. Muquet, R. Hassani, and F. Renard (2005), Experimental microstylolites
 926 in quartz and modeled application to natural stylolitic structures, *J. Struct. Geol.*, *27*,
 927 89–100.

928 Grinfeld, M. A. (1986), Instability of the interface between a nonhydrostatically stressed
 929 elastic body and a melt, *Sov. Phys. Dokl.*, *31*, 831.

930 Gunzburger, Y., and F. H. Cornet (2007), Rheological characterization of a sedimentary
 931 formation from a stress profile inversion, *Geophys. J. Int.*, *168*, 402–418.

932 Heald, M. T. (1955), Stylolites in sandstones, *J. Geol.*, *63*, 101–114.

933 Iijima, A. (1979), Nature and origin of the Paleogene cherts in the Setogawa Terrain,
 934 Shizuoka, central Japan, *J. Fac. Sci. Univ. Tokyo, Sect. 2*, *20*, 1–30.

935 Karcz, Z., E. Aharonov, D. Ertas, R. Polizzotti, and C. H. Scholz (2008), Deformation by
 936 dissolution and plastic flow of a single crystal sodium chloride indenter: an experimental
 937 study under the confocal microscope, *J. Geophys. Res.*, *113*, b04205.

938 Kassner, K., C. Misbah, J. Müller, J. Kappey, and P. Kohlert (2001), Phase-field modeling
 939 of stress-induced instabilities, *Phys. Rev. E*, *63*, 036117.

940 Katsman, R. (2010), Extensional veins induced by self-similar dissolution at stylolites:
 941 analytical modeling, *Earth and Planet. Sci. Lett.*, *299*, 33–41.

942 Katsman, R., E. Aharonov, and H. Scher (2006a), A numerical study on localized volume
 943 reduction in elastic media: some insights on the mechanics of anticracks, *J. Geophys.*
 944 *Res.*, *111*, b03204.

945 Katsman, R., E. Aharonov, and H. Scher (2006b), Localized compaction in rocks: Esh-
 946 lely's inclusion and the Spring Network Model, *Geophys. Res. Lett.*, *33*, 110311.

947 Koehn, D. (2012), personal comm.

948 Koehn, D., J. Arnold, B. Jamtveit, and A. Malthe-Sørenssen (2003), Instabilities in stress
 949 corrosion and the transition to brittle failure, *American J. Sci.*, *303*, 956–971.

950 Koehn, D., D. K. Dysthe, and B. Jamtveit (2004), Transient dissolution patterns on
 951 stressed crystal surfaces, *Geochimica et Cosmochimica Acta*, *68*, 3317–3325.

952 Koehn, D., F. Renard, R. Toussaint, and C. W. Passchier (2007), Growth of stylolite
 953 teeth patterns depending on normal stress and finite compaction, *Earth and Planet.*
 954 *Sci. Lett.*, *257*, 582–595.

955 Landau, L. D., and E. M. Lifchitz (1986), *Theory of elasticity*, Butterworth-Heinemann-
 956 London, 3rd ed.

957 Laronne Ben-Itzhak, L. (2011), *Pressure solution and stylolites in carbonate rocks*, *Ph.D.*
 958 *dissertation thesis*, Weizmann Institute of Sciences, Rehovot.

959 Lind, I. L. (1993), Stylolites in chalk from leg 130, Ontong Java Plateau, *Proc. ODP Sci.*
 960 *Results*, *130*, 673–686.

961 Misbah, C., F. Renard, J. P. Gratier, and K. Kassner (2004), Dynamics of a dissolution
 962 front for solids under stress, *Geophys. Res. Lett.*, *31*, 106618.

963 Mollema, P. N., and M. A. Antonellini (1996), Compaction bands: a structural analog for
 964 anti-mode I crack in aeolian sandstone, *Tectonophysics*, *267*, 209–228.

965 Park, W. C., and E. H. Schot (1968), Stylolites: their nature and origin, *J. Sediment.*
 966 *Petrol.*, *38*, 175–191.

967 Railsback, L. B. (1993), Lithologic controls on morphology of pressure-dissolution surfaces
 968 (stylolites and dissolution seams) in Paleozoic carbonate rocks from the mideastern
 969 United States, *J. Sed. Res.*, *63*, 513–522.

970 Renard, F., P. Ortoleva, and J. P. Gratier (1997), Pressure solution in sandstones: influ-
 971 ence of clays and dependence on temperature and stress, *Tectonophysics*, *280*, 257–266.

972 Renard, F., D. Dysthe, J. Feder, K. Bjørlykke, and B. Jamtveit (2001), Enhanced pressure
 973 solution creep rates induced by clay particles: experimental evidence in salt aggregates,
 974 *Geophys. Res. Lett.*, *28*, 1295–1298.

975 Renard, F., J. Schmittbuhl, J. P. Gratier, P. Meakin, and E. Merino (2004), Three-
 976 dimensional roughness of stylolites in limestones, *J. Geophys. Res.*, *109*, b03209.

977 Rispoli, R. (1981), Stress field about strike-slip faults inferred from stylolites and tension
 978 gashes, *Tectonophysics*, *75*, 29–36.

979 Roux, S., and A. Hansen (1994), Interface roughening and pinning, *J. Phys. I (France)*,
 980 *4*, 515–538.

981 Rutter, E. H. (1976), The kinetics of rock deformation by pressure solution, *Philos. Trans.*
 982 *R. Soc. London Ser.A*, *283*, 203–219.

983 Rutter, E. H. (1983), Pressure solution in nature, theory and experiment, *J. Geol. Soc.*,
 984 *140*, 725–740.

985 Schmittbuhl, J., F. Schmitt, and C. Scholz (1995), Scaling invariance of crack surfaces, *J.*
 986 *Geophys. Res.*, *100*, 5953–5973.

987 Schmittbuhl, J., F. Renard, J. P. Gratier, and R. Toussaint (2004), Roughness of stylolites:
 988 implications of 3D high resolution topography measurements, *Phys. Rev. Lett.*, *93*,
 989 238501.

990 Schutjens, P., and C. Spiers (1999), Intergranular pressure solution in NaCl: Grain-to-
 991 grain contact experiments under the optical microscope, *Oil Gas Sci. Technol.*, *54*, 729.

992 Simonsen, I., A. Hansen, and O. M. Nes (1998), Determination of the Hurst exponent by
 993 use of wavelet transforms, *Phys. Rev. E*, *58*, 2779–2787.

994 Stockdale, P. B. (1922), Stylolites: their nature and origin, *Indiana University Studies*, *9*,
 995 1–97.

996 Stockdale, P. B. (1926), The stratigraphic significance of solution in rocks, *J. Geol.*, *34*,
 997 399–414.

998 Stockdale, P. B. (1936), Rare stylolites, *American J. Sci.*, *32*, 129–133.

999 Stockdale, P. B. (1943), Stylolites: primary or secondary?, *J. Sediment. Petrol.*, *13*, 3–12.

1000 Stutzer, O. (1940), *Geology of coal*, Univ. Chicago Press.

1001 Tanguy, A., M. Gounelle, and S. Roux (1998), From individual to collective pinning:
 1002 Effect of long-range elastic interactions, *Phys. Rev. E*, *58*, 1577–1590.

1003 Tembe, S., P. Baud, and T. Wong (2008), Stress conditions for the propagation of discrete
 1004 compaction bands in porous sandstone, *J. Geophys. Res.*, *113*, b09409.

1005 Wileveau, Y., F. H. Cornet, J. Desroches, and P. Blumling (2007), Complete in situ stress
 1006 determination in an argillite sedimentary formation, *Phys. Chem. Earth*, *32*, 866–878.

1007 Wright, T. O., and L. B. Platt (1982), Pressure dissolution and cleavage in Martingsburg
 1008 shale, *American J. Sci.*, *282*, 122–135.

1009 Young, R. B. (1945), Stylolitic solution in Wit-watersrand quartzites, *Geol. Soc. S. Afr.*
1010 *Trans.*, 47, 137–142.

1011 Zhou, X., and A. Aydin (2010), Mechanics of pressure solution seam growth and evolution,
1012 *J. Geophys. Res.*, 115, b12207.

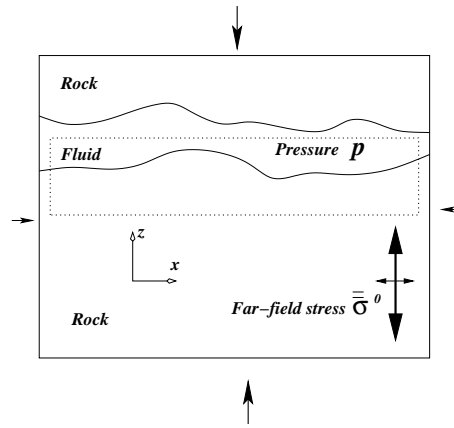


Figure 1. Initial stage of a stylolite: Trapped elongated fluid pocket.

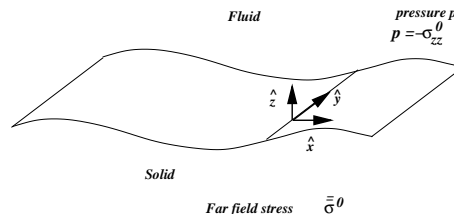


Figure 2. Solid-fluid interface: geometry considered.

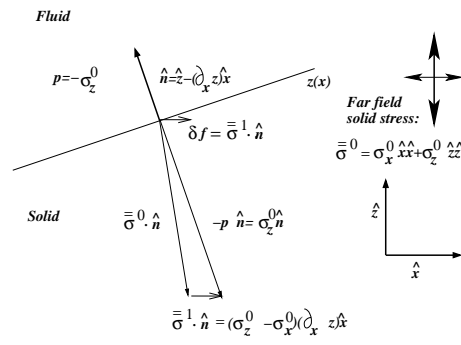


Figure 3. Local mechanical equilibrium along the fluid-solid interface (equation 8).

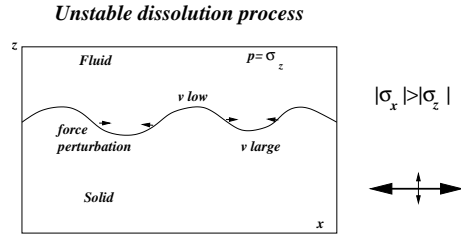


Figure 4. Surface tangential to the largest stress (σ_{xx}) axis: unstable case, Azaro-Tiller-Grinsfeld instability.

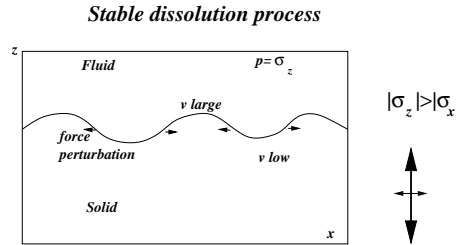


Figure 5. Surface normal to the largest stress (σ_{zz}) axis: stable case.

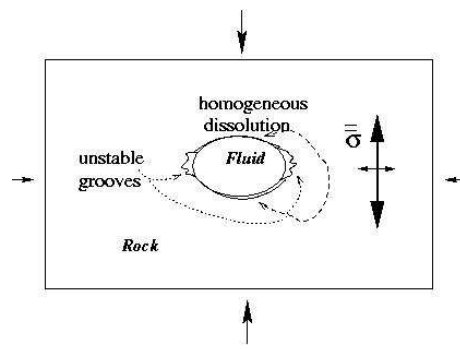


Figure 6. Expected stability or instability of the dissolution front around a trapped fluid pocket.

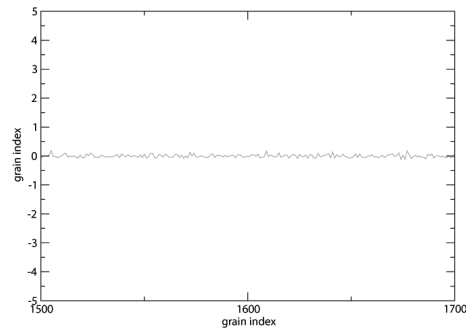


Figure 7. Snapshot of the pressure-solution profile.

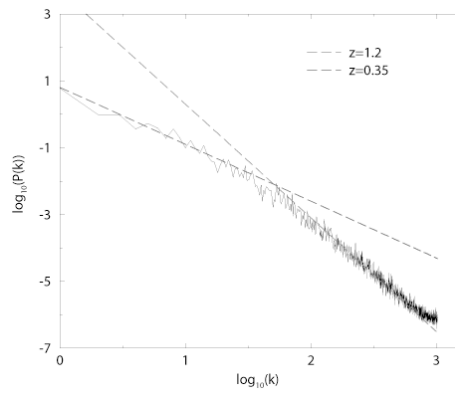


Figure 8. Average power spectrum of simulated stylolitic fronts, in bilogarithmic representation. The k -unit is $2\pi/L$, with $L = 4096\ell$ and a grain size $\ell = 10\mu\text{m}$. The vertical unit is arbitrary. The crossover is obtained at $2\pi/L^*$.

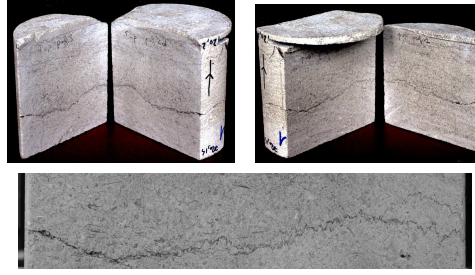


Figure 9. Profiles 1, 2, 3 and 4 from right to left. A core from the Dogger formation (EST433 well) was cut in three parts to obtain four profiles. Each profile was photographed at high resolution. The picture at the bottom shows the profile number 2.

Profile number	1	2	3	4	Average, \bar{L}^*
L_{FPS}^* (mm)	1.14	0.37	0.37	1.13	0.75 ± 0.51
L_{AWC}^* (mm)	1.95	1.52	0.72	1.60	1.45 ± 0.64

Table 1. Summary of the cross-over length found for the four profiles analyzed by Fourier power spectrum (FPS) and average wavelet coefficient (AWC).

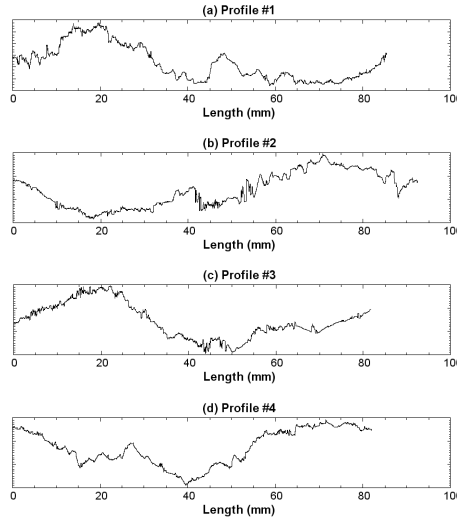


Figure 10. Functions obtained from profiles 1, 2, 3 and 4. A grey-level threshold was imposed on the pictures to isolate the stylolites. The functions were then obtained by selecting the mean limit of the pixels.

$\gamma(J \cdot m^{-2})$	$E_{up}(GPa)$	ν	α	β
0.27	36.2±0.4	0.37±0.04	0.32±0.01	0.033±0.007

Table 2. Summary of the estimated paleostress for the stylolites from the cross-over length.

Paleostress (MPa)	\bar{L}^*, E_{low}	\bar{L}^*, E_{up}
σ_{FPS}	22.6±14.9	35.1±23.2
σ_{AWC}	16.3±8.8	25.3±13.7

Table 3. Results for the calculation of the paleostress σ_{zz} using the averaged cross-over length for the Fourier power spectrum (FPS) and average wavelet coefficient (AWC) methods. We calculated the paleostress taking into account the variability of the Young's modulus E where E_{low} is the lower limit for the Young's modulus for limestones and E_{up} is the determined Young's modulus for the studied sample.

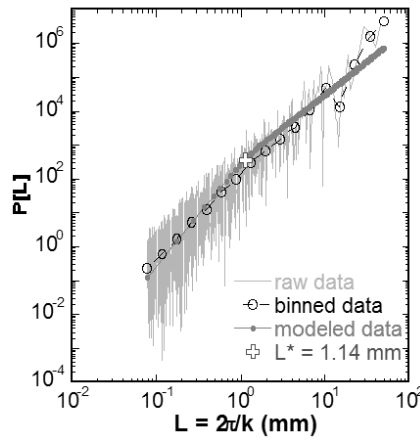


Figure 11. Fourier power spectrum of the profile 1. The raw data were binned logarithmically to run a linear-by-part fitting on the data [Ebner *et al.*, 2009b]. Two different scaling regimes are observed at small and large scale with Hurst exponent around 1 and 0,5 respectively. The fit reveals a cross-over length L^* around 1.14 mm.

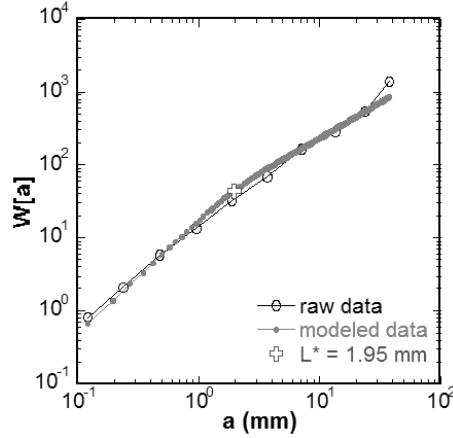


Figure 12. Averaged wavelet coefficient spectrum of the profile 1. A linear-by-part fitting were run on the data [Ebner *et al.*, 2009b]. Two different scaling regimes are observed at small and large scale with Hurst exponent around 1 and 0.5 respectively. The fit reveals a cross-over length L^* around 1.95 mm. This is in good agreement with the length inferred using the Fourier power spectrum method.

Depth (m)	\bar{L}^*, E_{low}	\bar{L}^*, E_{up}
h_{FPS}	850.1±561.1	1320.3±871.4
h_{AWC}	613.1±331.1	951.7±513.9

Table 4. Results for the calculation of the depth for the Fourier power spectrum (FPS) and average wavelet coefficient (AWC) methods. We consider an early stage of formation of a sedimentary basin with an overburden made of limestones only.